Hasani et al. *NPG Asia Materials* (2019) 11:47
https://doi.org/10.1038/s41427-019-0145-7

NPG Asia Materials

ARTICLE Open Access

Direct synthesis of two-dimensional MoS_2 on *p*-type Si and application to solar hydrogen production

Amirhossein Hasani[1], Quyet Van Le[2], Mahider Tekalgne[1], Min-Ju Choi[3], Tae Hyung Lee[3], Ho Won Jang[3] and Soo Young Kim[4]

Abstract

Transition metal dichalcogenides (TMDs) are promising two-dimensional (2D) materials, and MoS_2 has been specifically utilized in electronic devices and integrated circuits. However, the direct synthesis of MoS_2 on traditional semiconductors, such as silicon, remains challenging due to the hydrophobic surface of nonoxide wafers (e.g., Si, GaAs, and InP). Herein, a novel, facile, reliable, and one-step method for the direct synthesis of single-crystal MoS_2 on a *p*-Si wafer via hybrid thermolysis is proposed. To demonstrate the applicability of the proposed method, a MoS_2/*p*-Si heterojunction was fabricated and used for solar-driven hydrogen production. The as-fabricated *n*-MoS_2/*p*-Si heterojunction exhibited a benchmark current density of -13.5 ± 1 mA/cm^2 at 0 V and an onset potential of +0.02 V. This method reliably and efficiently produced high-quality MoS_2 crystals on a wafer scale and is sufficiently simple to overcome the challenges associated with previous approaches. The method developed herein represents a tremendous advancement in the fabrication of 2D electronic devices.

Introduction

The discovery of low-dimensional materials represents a key point in the progress of electronic device development[1–4]. Emerging transition metal dichalcogenides (TMDs) have revolutionized two-dimensional (2D) semiconductor-based electronics due to their unique optical, electronic, and mechanical properties. TMDs have great potential to be utilized in various applications, including solar cells, light-emitting diodes (LEDs), gas sensors, photocatalysis systems, and photodetectors[5–9].

Recently, TMDs such as MoS_2, WS_2, $MoSe_2$, and WSe_2 have been introduced for use in different applications[10–13]. Among these TMDs, the n-type semiconductor MoS_2 has been most extensively studied owing to its remarkably tunable optoelectronic and photochemical properties with a direct band gap of 1.8 eV, making it a promising low-dimensional material for future optoelectronic devices[3,14]. For over a decade, a variety of synthesis methods for MoS_2 have been proposed using chemical vapor deposition (CVD), hydrothermal, sputtering, epitaxial growth, and thermolysis methods[15–19]. However, the fabrication of large-scale, uniform, and high-quality crystalline MoS_2 remains challenging.

The elementary building blocks of p–n junctions are vital for semiconductor electronic devices such as integrated circuits, photodetectors, solar cells, LEDs, diodes, and transistors[20–24]. Recently, the integration of low-dimensional TMD materials with single-crystal traditional semiconductors (e.g., Si, GaAs, and InP) has significantly impacted the development of functional electronic

Correspondence: Soo Young Kim (sooyoungkim@cau.ac.kr) or Ho Won Jang (hwjang@snu.ac.kr)
[1]School of Chemical Engineering and Materials Science, Integrative Research Center for Two-Dimensional Functional Materials, Institute of Interdisciplinary Convergence Research, Chung-Ang University, 84 Heukseok-ro, Dongjak-gu, Seoul 06974, Republic of Korea
[2]Institute of Research and Development, Duy Tan University, Da Nang 550000, Vietnam
Full list of author information is available at the end of the article.
These authors contributed equally: Amirhossein Hasani, Quyet Van Le

devices, including field effect transistors (FETs), diodes, photodetectors, and photoelectrochemical cells[21,25–27]. However, poor-quality TMD-based heterojunctions and difficulty in large-scale fabrication restrict commercial applications. For example, so-called native oxides form easily on the Si wafer surface, resulting in poor contact with MoS_2 and deteriorated device performance. Therefore, the large-scale synthesis of superpristine MoS_2 on Si wafers has yet to be achieved.

Generally, two procedures are used for the fabrication of p–n heterojunctions in 2D TMD materials and Si: (1) synthesis of TMDs on SiO_2 and subsequent transfer to arbitrary substrates such as Si, GaAs, and InP wafers and (2) direct synthesis of TMDs on an arbitrary substrate[25,27,28]. To the best of our knowledge, extensive research on the transfer process has been performed[29–31]. For example, Kwon et al. fabricated a p–n heterojunction using n-MoS_2 and p-Si for use in photoelectrochemical hydrogen production[27]. The fabrication process involved wet transferring, where MoS_2 was initially grown on SiO_2/Si and subsequently transferred to p-Si using a supporting layer and removal process. Despite the efficient performance obtained, the fabrication of p–n heterojunctions is not easily reproducible because the transfer process is challenging and time-consuming for n-MoS_2/p-Si heterojunctions. On the other hand, the only method for the direct synthesis of TMDs on Si is the sputtering method. Hao et al. fabricated MoS_2/Si p–n junctions using the DC magnetron technique for use in photovoltaic cells[25]. However, the sputtering method for the direct synthesis of MoS_2 on p-Si results in poor MoS_2 crystallinity, and the formation of the MoS_2 film on p-Si is not easily controlled. Therefore, significant demand exists for the development of a reliable method for 2D p–n junction fabrication. The proposed method should be a wafer-scale, simple, fast (no transfer step), reproducible method that produces highly crystalline TMD films.

Herein, we report a novel method for the direct synthesis of 2D layered MoS_2 on a p-Si substrate, representing a tremendous advancement in the fabrication of 2D electronic devices, overcoming the challenges of previously reported techniques[27,32,33]. We demonstrate an approach for the direct synthesis of wafer-scale MoS_2 on p-Si using thermolysis to achieve perfect crystals. This method can be more broadly applied to other TMDs and single-crystal wafers. In addition, to show the applicability of the developed method, the as-fabricated n-MoS_2/p-Si heterojunction was used for photoelectrochemical hydrogen production. Because of the direct formation of superpristine MoS_2 on p-Si and the high-quality p–n heterojunctions formed, the as-prepared photocathode exhibited efficient performance with a high current density of -13.5 ± 1 mA/cm^2 at 0 V and an onset potential of +0.02 V. The direct fabrication of p–n heterojunctions prepared using the proposed method offers a facile, reliable, time-saving fabrication process representing a remarkable development for the production of high-quality semiconductor electronic devices.

Direct synthesis of MoS_2 on p-Si

Thermolysis of ammonium tetrathiomolybdate ($(NH_4)_2MoS_2$)) was used to form the MoS_2 thin film. Preparation of large-scale and high-quality MoS_2 by thermolysis is an efficient and facile approach that is well documented in the literature[27,34,35]. Liu et al. synthesized MoS_2 using thermal decomposition of an $(NH_4)_2MoS_4$ layer in the presence of sulfur[34]. Similarly, Kwon et al. used the same process to fabricate high-quality MoS_2[27]. To date, the decomposition of the $(NH_4)_2MoS_2$ layer at high temperatures to form MoS_2 thin films has mostly involved the use of a SiO_2/Si substrate. In this study, the $(NH_4)_2MoS_4$ precursor was coated on a SiO_2/Si substrate and subsequently annealed in the presence of sulfur to form MoS_2/SiO_2/Si. Coating of the $(NH_4)_2MoS_2$ precursor on a substrate with a hydrophobic surface, such as p-Si, is impossible so we used a hybrid method to directly synthesize MoS_2 on the p-Si substrate. As shown schematically in Fig. 1a, MoO_3 with different thicknesses (5, 10, 15, and 20 nm) was deposited onto the p-Si substrate via evaporation to increase the hydrophilicity of the Si substrate. The $(NH_4)_2MoS_2$ solution was then coated onto MoO_3/p-Si via spin coating. Finally, the $(NH_4)_2MoS_4$/MoO_3/p-Si was converted to MoS_x/p-Si at 500 °C under H_2 and N_2 gas flow via thermolysis (Fig. 1b). Finally, the temperature was raised to 900 °C to transform the MoS_x layer to a MoS_2 thin film and fabricate the MoS_2/p-Si heterojunctions. It is clear from Fig. 1c that the contact angle of $(NH_4)_2MoS_4$ with p-Si is quite high (55.5°), suggesting a poorly hydrophilic surface and the impossibility of coating the $(NH_4)_2MoS_4$ solution on p-Si (Fig. 1c, left). On the other hand, the p-Si surface could be converted to a super-hydrophilic surface after MoO_3 deposition, allowing the $(NH_4)_2MoS_4$ precursor to be easily coated on the substrate (Fig. 1c, right). To show the successful coating of the $(NH_4)_2MoS_4$ precursor on p-Si, a video was recorded before and after MoO_3 deposition (Video S1, S2). Figure 1d shows the wafers of the directly fabricated MoS_2/p-Si heterojunction, highlighting the efficiency and ease of the proposed method. Using this method, the large-scale fabrication of 2D-based semiconductor devices and integrated circuits could be achieved.

Results and discussion

The uniformity of 2D-TMD materials is an important parameter that directly affects device performance. Methods such as sputtering, epitaxial growth, and thermolysis have been proposed for the fabrication of large-

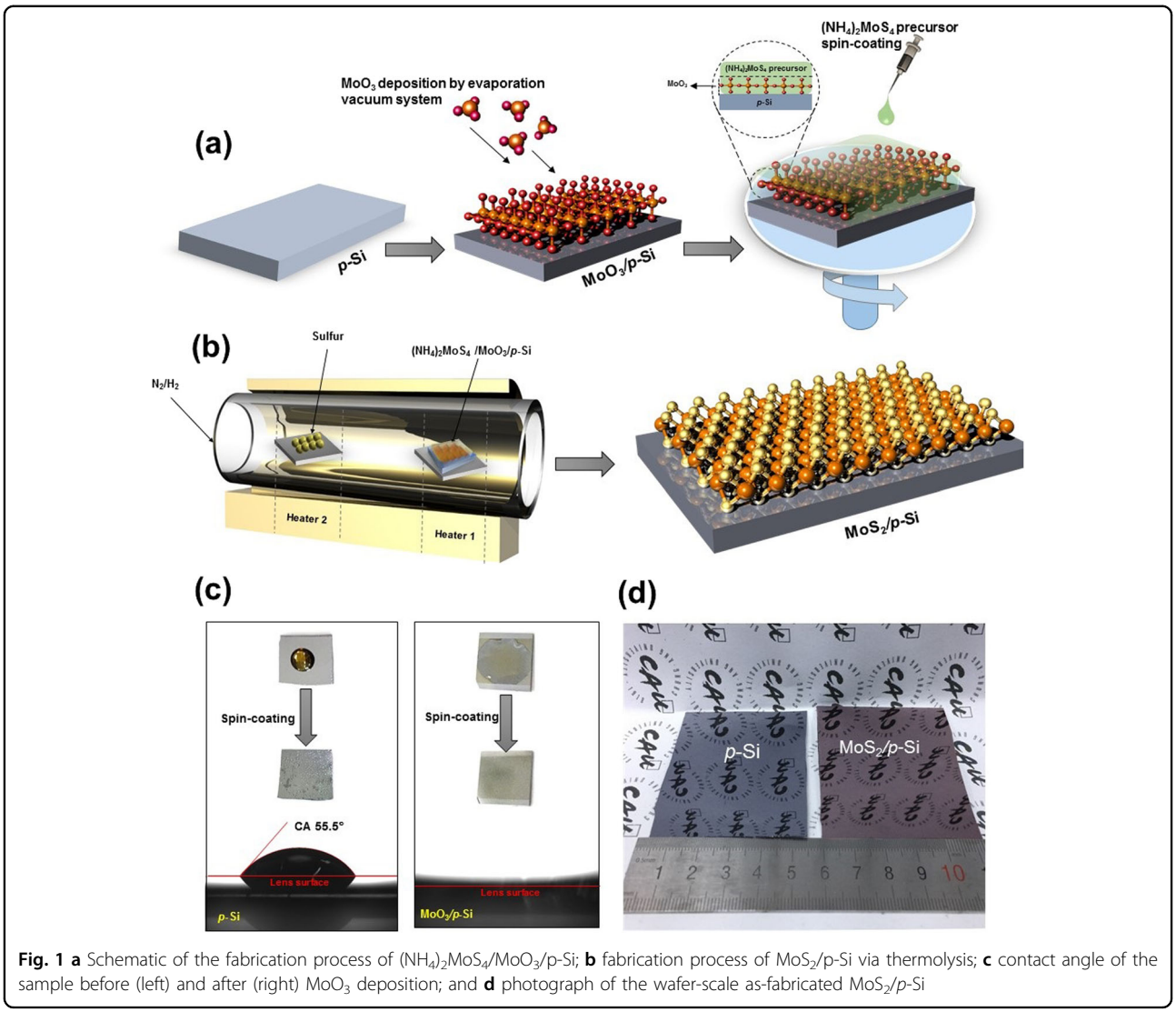

Fig. 1 a Schematic of the fabrication process of $(NH_4)_2MoS_4/MoO_3$/p-Si; **b** fabrication process of MoS_2/p-Si via thermolysis; **c** contact angle of the sample before (left) and after (right) MoO_3 deposition; and **d** photograph of the wafer-scale as-fabricated MoS_2/*p*-Si

scale and uniform MoS_2. Dumcenco et al. demonstrated the growth of monolayer MoS_2 via epitaxial growth[36]. However, randomly triangular-shaped MoS_2 with uncontrollable orientation limited the reliability of their process and prevented commercialization.

Atomic force microscopy (AFM) was used to examine the topological properties and thickness of the MoS_2 thin films. The inset of Fig. 2a shows the morphology of the as-obtained thickness (11 nm) of the 10 nm MoO_3 deposited on p-Si, which is attributed to the incorporation of $(NH_4)_2MoS_4$ and MoO_3 layers to form the MoS_2 thin film. The roughness of MoS_2 was 2.4 Å for the 10 nm MoO_3 deposited on p-Si (Fig. 2a), which is one of the smallest reported values to the best of our knowledge[27,37]. These results confirm that the MoS_2 thin film on p-Si obtained using this method is superpristine and ultraclean, resulting in high-quality p–n heterojunctions and enhanced device performance. Furthermore, AFM was performed to evaluate the roughness and thickness under various conditions (Fig. S1) and confirmed the controllability of the developed method. The results demonstrate that the MoS_2 thickness can be easily controlled by the deposition of MoO_3, obtaining MoS_2 thicknesses of approximately 8.5, 11, 16.8, and 25.2 nm for the 5, 10, 15, and 20 nm MoO_3 depositions on p-Si, respectively (Fig. 2b). In addition, the lowest roughness of 2.4 Å was obtained for the 11 nm MoS_2 film, which would likely provide the best device performance. From the AFM results, the film roughness can be optimized by adjusting the MoO_3 thickness on p-Si. Field-emission scanning electron microscopy (FE-SEM) was used to examine the morphology of the MoS_2 thin film on the p-Si substrate (Fig. 2c). From the FE-SEM images of the as-synthesized MoS_2 films, the films were uniform and continuous over the entire surface of the p-Si substrate. Moreover, Fig. S2a–d shows the as-synthesized MoS_2 on p-Si with different

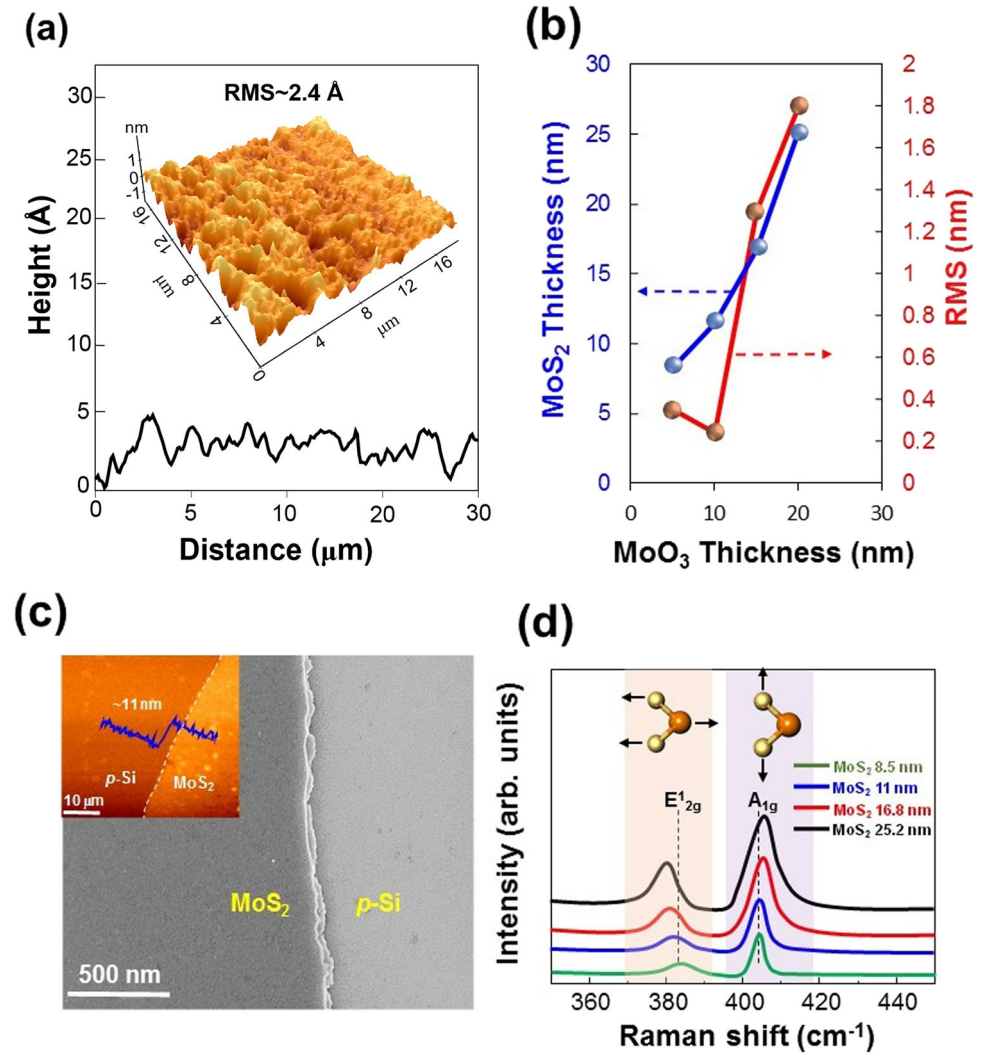

Fig. 2 a Roughness measurements of the as-fabricated MoS_2/p-Si using 10 nm deposited MoO_3; **b** thicknesses and roughness values of the MoS_2 thin films as a function of MoO_3 thickness; **c** FE-SEM image and AFM thickness measurement (inset) of the MoS_2(11 nm)/*p*-Si sample; and **d** Raman spectra of the as-prepared MoS_2 thin films with different thicknesses

MoO_3 thicknesses (5, 10, 15, and 20 nm). Figure 2d shows the Raman spectra of the MoS_2 thin films with different thicknesses. Two vibrational modes (A_{1g} and E^1_{2g}) were observed and attributed to the out-of-plane and in-plane stretching, respectively[38]. The distance between A_{1g} and E^1_{2g} increased with an increase in the thickness of the MoS_2 film, which was attributed to the tightening of the A_{1g} mode and moderation of the E^1_{2g} mode[27]. To confirm the formation of the MoS_2 thin film and the impossibility of MoS_2/MoO_3, Raman analysis was utilized for the as-synthesized MoS_2 thin film and as-deposited MoO_3 layer (see Fig. S3). Two dominant peaks (A_{1g} and E^1_{2g}) are located at 383 and 404 cm^{-1} in the as-prepared MoS_2, while two dominant peaks are located at 820 and 997 cm^{-1} in MoO_3. Therefore, the possibility of the existence of MoO_3 in the as-direct synthesized MoS_2 can be excluded.

X-ray diffraction (XRD) measurements were used to confirm the ultrahigh purity of the 2H-MoS_2 single crystal on p-Si (Fig. 3a). The corresponding peaks were sharp and located at 14.5 and 63.8°, arising from the (002) and (008) planes, respectively. Patil et al. evaluated the crystal structure of bulk MoS_2 and thin film MoS_2[15]. The bulk MoS_2 showed various peaks, whereas the as-prepared MoS_2 showed only a (002) peak, and the other peaks were diminished, suggesting a highly pristine MoS_2 single-crystal layer. High-resolution transmission electron microscopy (HR-TEM) was used to confirm the quality of the MoS_2 crystal, and the result is shown in the inset of Fig. 3a. The 2H-phase of MoS_2 was observed mainly with

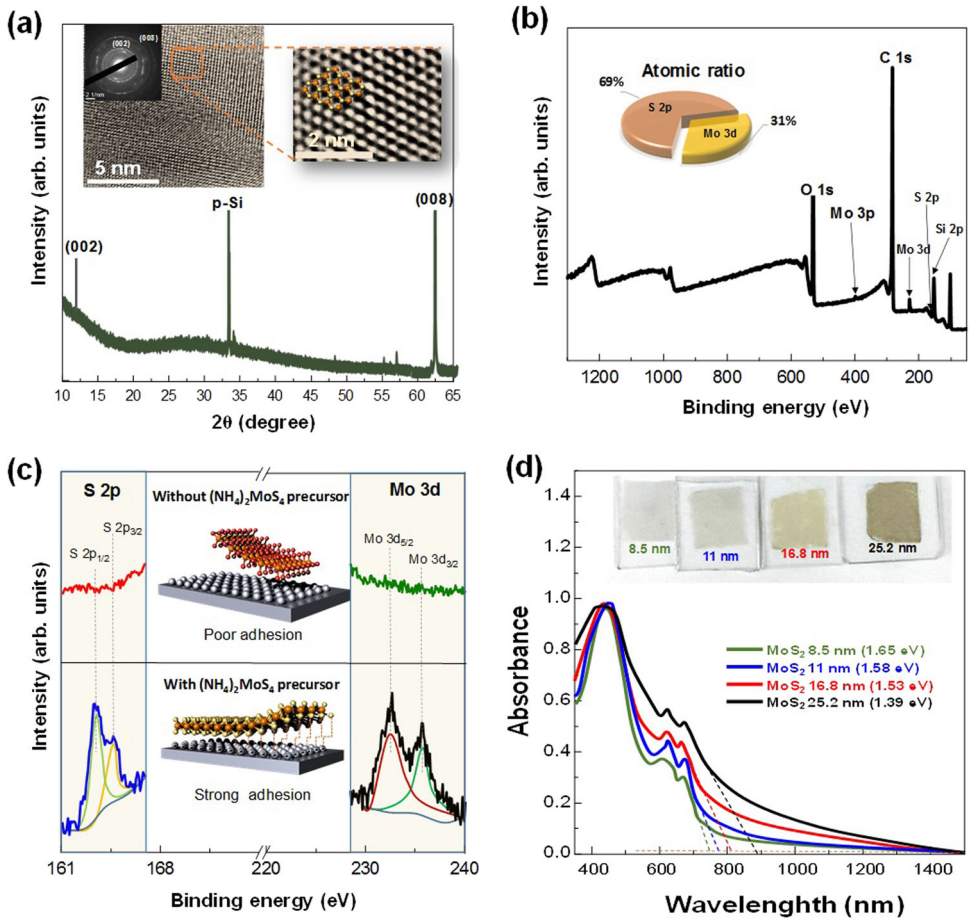

Fig. 3 a XRD spectra and HR-TEM measurements (inset) of the as-fabricated MoS_2 (11 nm)/p-Si sample; **b** wide range XPS spectra of the as-fabricated MoS_2 (11 nm)/p-Si sample and the corresponding atomic ratio; **c** high-resolution Mo and S peaks for the MoS_2/*p*-Si samples prepared with and without the $(NH_4)_2MoS_4$ layer; and **d** absorbance spectra of the as-prepared MoS_2 thin films on glass with different thicknesses

[002] and [008] orientations (inset of Fig. 3a), which was completely confirmed by the XRD results. From the XRD data, three sharp domain peaks were observed and were ascribed to the highly crystalline MoS_2 film on *p*-Si. X-ray photoelectron spectroscopy (XPS) was used to determine the elemental composition, and the atomic ratios of the samples are shown in Fig. 3b. The XPS spectra are shown in Fig. 3b, confirming the presence of Mo and S and successful formation of the MoS_2 film. In addition, the ratio of Mo to S was 31:69, which approximately agrees with the MoS_2 structure (inset of Fig. 3b). The high-resolution XPS peaks of S 2p and Mo 3d are shown in Fig. 3c. To study the effects of the $(NH_4)_2MoS_4$ precursor on the formation of single-crystal MoS_2 on p-Si, XPS was performed on the MoS_2 prepared with and without the $(NH_4)_2MoS_4$ precursor. Because of the very weak bonds between the deposited MoO_3 layer and the *p*-Si substrate, no peaks originating from Mo or S were observed without the precursor (see Fig. 3c, red and green curves). On the other hand, the Mo 3d and S 2p peaks were strongly apparent after deposition of the $(NH_4)_2MoS_4$ precursor on MoO_3/*p*-Si. The $(NH_4)_2MoS_4$ precursor assists in the formation of MoS_2 and likely acts as a protective layer to prevent evaporation of the MoO_3 layer during thermolysis. In previous studies, this phenomenon has been attributed to the higher O-S bonding energy compared to that of the Si-S bond[27,39]. However, we believe that the poor hydrophilicity of the Si wafer is the main reason underlying the impossibility of direct growth of MoS_2 crystals on nonoxide wafers. The UV-vis normalized absorbance of the different thicknesses of the as-transferred MoS_2 thin films on glass are shown in Fig. 3d. The optical band gaps were evaluated via prolonging the line of the initial absorbance peak and increased from 1.39 to 1.65 eV as the layer thickness decreased from 25.2 to 8.5 nm. Additionally, the as-transferred MoS_2 layers with different thicknesses on glass are shown in the inset of Fig. 3d. The films uniformly covered the glass substrate, and the film color changed from transparent to dark brown with an increase in

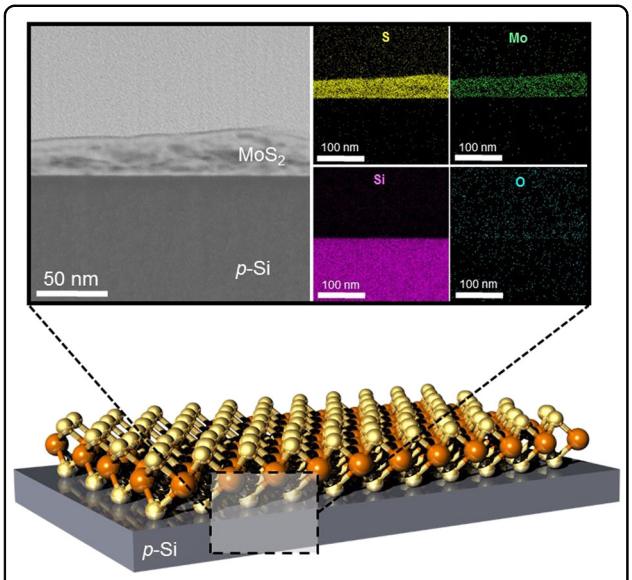

Fig. 4 Cross-sectional STEM images of the synthesized MoS2 on p-Si and energy-dispersive X-ray spectroscopy (EDS) mapping for the MoS_2/p-Si heterostructure

thickness from 8.5 to 25.2 nm. These results confirmed that the optical and electronic properties can be easily tuned via the proposed method, which is more reliable and reproducible than previously developed methods[29,31–33].

The crystalline structure of the vertical cross-section of the MoS_2 film was examined by TEM (see Fig. 4). TEM with energy-dispersive X-ray spectroscopy (TEM-EDS) mapping of the as-direct synthesized MoS_2 thin film showed Mo and S constituting the MoS_2 crystalline structure were uniformly distributed throughout the film. However, there was some O due to air oxidation of the sample. Therefore, the results confirm the formation of MoS_2/p-Si, and the possibility of MoS_2/MoO_3/p-Si is excluded.

To confirm the applicability of this method, a MoS_2/p-Si photocathode was fabricated, and it is clear that the most difficult and time-consuming step (the transfer process) was removed to improve upon previously reported methods[27,29,31]. The as-fabricated photocathode was used as a working electrode in a three-electrode electrochemical cell filled with 0.5 M sulfuric acid as an electrolyte and was placed under simulated solar irradiation (100 mW/cm^2). Figure 5a shows the photocurrent onset potential (RHE) vs. current density of the sample under different conditions, confirming the successful fabrication of a MoS_2/p-Si heterojunction that showed p–n junction behavior. The dark current is shown as the violet-color line. The cost-effective fabrication procedure of bare p-Si, as well as its suitable band gap and crystallinity, are particularly suited for solar hydrogen production[27,40]. However, to absorb H_2 onto the p-Si surface, a very large voltage must be applied. Therefore, the integration of a catalyst, such as 2D-TMDs, with p-Si must be performed to achieve efficient hydrogen production performance. MoS_2 (11 nm)/p-Si showed the highest performance with a current density benchmark of -13.5 ± 1 mA/cm^2 at 0 V and an onset potential of +0.02 V, which is significantly improved over that of bare p-Si (0.2 mA/cm^2 at 0 V and an onset potential of −0.38 V). To investigate the mechanism and catalytic activity of the MoS_2 layers, current density-potential polarization curves were translated to the logarithmic value of the current density as a function of the overpotential (Fig. 5b). From the photoelectrochemical (PEC) measurement results, the MoS_2 (11 nm)/p-Si sample is expected to exhibit the highest catalytic activity. MoS_2 (11 nm)/p-Si exhibited the lowest Tafel slope of 65 mV/dec, which corresponds to the Volmer–Heyrovsky electrochemical mechanism[41]. These results show that the optimization of the MoS_2 layer thickness is essential for achieving the highest performance of the resulting devices. Since the proposed fabrication method is a controllable process, the resulting MoS_2 thin film can be easily optimized. Electrochemical impedance spectroscopy (EIS) is another method that can be used to evaluate photocatalytic activity. The small circle in the EIS Nyquist plot represents the figure of merit for the HER activity, as shown in Fig. 5c. From these EIS results, the smallest circle was obtained for the MoS_2 (11 nm)/p-Si sample, as expected. The fastest movement of electrons between the electrolyte and working electrode was obtained using the optimized MoS_2 (11 nm)/p-Si photocathode. The inset of Fig. 5c shows the Randles equivalent circuit including the active electrolyte resistance (R_S), charge-transfer resistance (R_{ct}), and capacitor. The value of R_{ct} was determined to be 66.5 Ω for the optimized MoS_2 (11 nm)/p-Si photocathode, agreeing with the current density results. Because the MoS_2 thin film is relatively transparent, the incident solar light passed through the film and was absorbed by *p*-Si, generating hole-electron pairs and current induction via electrons moving to the MoS_2 thin film and electrolyte. The stability of the as-optimized MoS_2 (11 nm)/p-Si photocathode was assessed for 20 cycles to clarify the durability of the device for the photoelectrochemical HER (see Fig. 5d). We found a negligible current density shift after 20 cycles ($\Delta J = \pm 1$ mA/cm^2), which confirmed the excellent stability of the as-fabricated MoS_2 (11 nm)/p-Si photocathode for solar hydrogen production. For the optimized MoS_2/p-Si photocathode, the current density was stable after 40 h without notable degradation, indicating that the synthesized MoS_2 thin film acts as not only a catalyst for hydrogen production but also an excellent passivation layer that prevents the *p*-Si photocathode from experiencing severe photocorrosion (see Fig. S4). Therefore, the optimized device prepared by the direct synthesis process

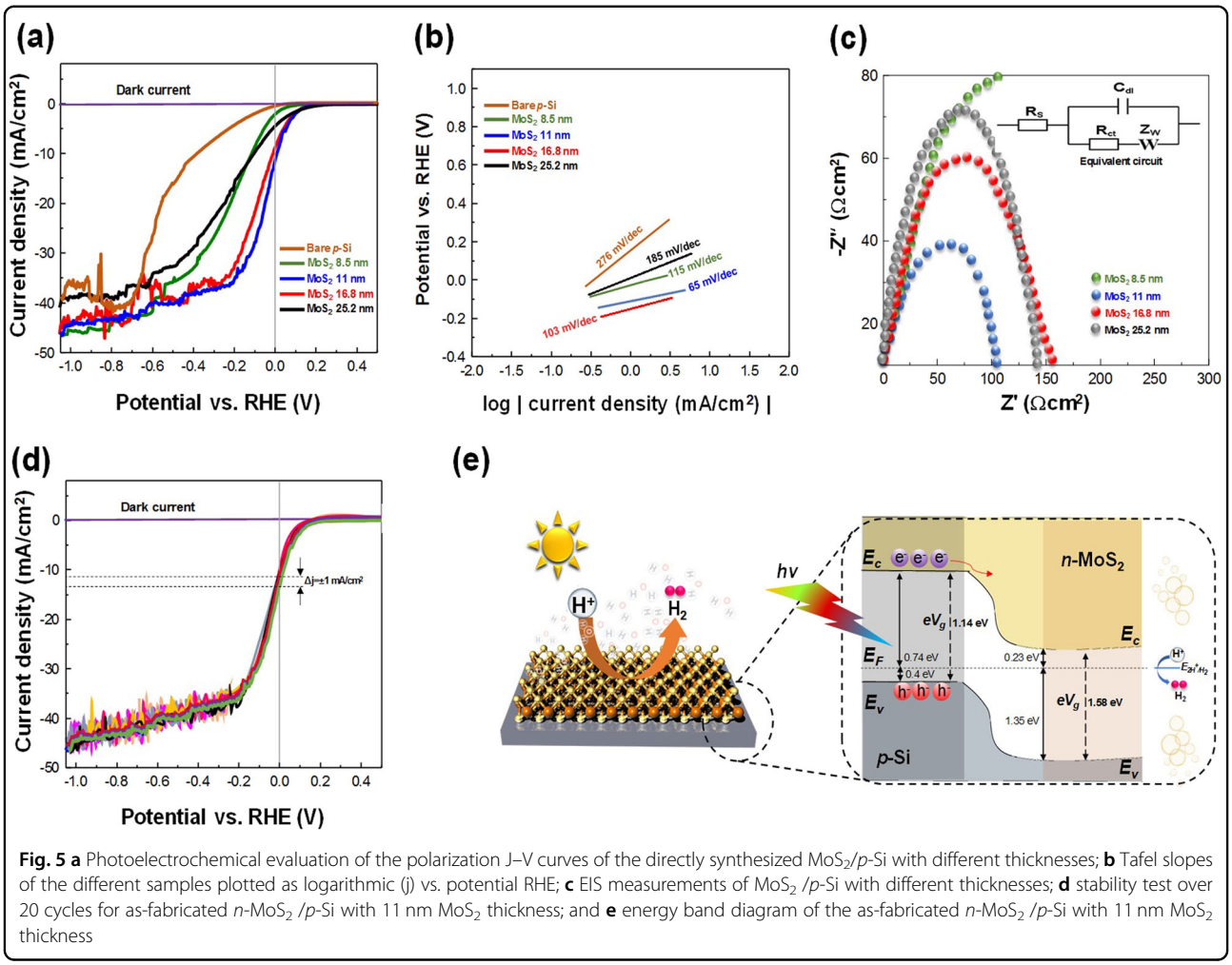

Fig. 5 a Photoelectrochemical evaluation of the polarization J–V curves of the directly synthesized MoS_2/*p*-Si with different thicknesses; **b** Tafel slopes of the different samples plotted as logarithmic (j) vs. potential RHE; **c** EIS measurements of MoS_2 /*p*-Si with different thicknesses; **d** stability test over 20 cycles for as-fabricated *n*-MoS_2 /*p*-Si with 11 nm MoS_2 thickness; and **e** energy band diagram of the as-fabricated *n*-MoS_2 /*p*-Si with 11 nm MoS_2 thickness

can be applied for long-term HER activity in acidic solutions under solar illumination. Ultraviolet photoelectron spectroscopy (UPS) measurements were performed to obtain the band diagram and energy levels, and the energy diagram of the optimized MoS_2/p-Si heterojunction is shown in Fig. 5e. From the UPS results, the work functions were determined to be 4.67 and 4.48 eV for the optimized MoS_2/p-Si and p-Si, respectively. From Fig. 5e, it is clear that for the optimized MoS_2, the Fermi level was located at 0.23 eV less than the conduction band (E_c), demonstrating n-type semiconductor behavior. The junction between the n- and p-type semiconductors resulted in band bending and Fermi level equalization. Therefore, the photogenerated carriers (electrons) were easily transferred from p-Si to the n-MoS_2 layer. In addition, the proximity of the E_c in MoS_2 to the hydrogen reduction potential ($E_{H+/H2} = 4.53$ eV) facilitated electron transfer from MoS_2 to the electrolyte without any significant obstacles.

The results show that the proposed method can provide a reliable and facile procedure for the fabrication of 2D material-based p–n junctions, which can be applied in an efficient manner. Table S1 indicates a comparison between the device performance of the as-direct synthesized MoS_2/*p*-Si photocathode with that of previously reported similar structures, current densities at 0 V vs. RHE and overpotentials for our MoS2/*p*-Si photocathode and other photocathodes based on 2D material /*p*-Si.

Conclusions

In conclusion, we developed a controllable method for the direct synthesis of MoS_2 on p-Si. Thermolysis is an efficient method for synthesizing MoS_2, but a superhydrophilic surface is required for the deposition of the $(NH_4)_2MoS_4$ precursor onto a nonoxide substrate. Therefore, we added an additional preliminary step (MoO_3 deposition) to convert the p-Si wafer from a poorly hydrophilic to a superhydrophilic surface for the precursor coating. The as-fabricated $MoO_3/(NH_4)_2MoS_4$/*p*-Si was successfully converted to MoS_2/p-Si via thermolysis. In addition, the MoS_2/p-Si heterojunction was used for solar hydrogen production to confirm the

applicability of the proposed method. The significant advantages of this controllable wafer-scale production process for the reproducible generation of highly crystalline products have the potential to revolutionize the 2D electronic industry in the near future.

Experimental section

Materials

All three chemicals used for the three-step cleaning process had purities exceeding 99.99% and were purchased from Sigma Aldrich Company. Hydrofluoric acid (HF, 10 vol%), MoO_3 powder (99.97% trace metals basis), ammonium tetrathiomolybdate (99.97% trace metals basis) and sulfur powder (99.98% purity) were purchased from Sigma Aldrich Company. Commercially available p-Si wafer, where p-Si specified with (100) orientation and p-type boron dopant, was used.

Methods

Fabrication of the MoS_2/p-Si heterojunction

First, *p*-Si wafers were cleaned ultrasonically using a conventional three-step process, followed by immersion in acetone, isopropyl, and deionized water. Next, the *p*-Si wafers were immersed in 10% hydrofluoric acid (HF, 10 vol%) to remove the native oxide. Subsequently, different thicknesses (5, 10, 15, and 20 nm) of MoO_3 were deposited onto p-Si using thermal evaporation. Next, a 10 mM solution of ammonium tetrathiomolybdate $(NH_4)_2MoS_4$ dissolved in glycol ethylene was spin coated onto the MoO_3/*p*-Si wafers at 4000 rpm for 60 s. Afterward, the samples were placed on a hot plate at 50 °C for 15 min to remove any remaining solvent. Subsequently, the MoO_3/*p*-Si wafers were placed in a CVD chamber to initiate thermolysis, and N_2 (200 cm^3/min) and H_2 (40 cm^3/min) gases were flowed in the chamber. Initially, the temperature was raised to 500 °C and was maintained for 30 min. The chamber pressure was maintained under the same N_2/H_2 gas flow at 1.2 Torr. Afterward, the chamber temperature was increased to 900 °C and maintained for 1 h. Finally, sulfurization was initiated using 0.5 g of sulfur powder (Sigma-Aldrich, 99.5% purity) in another heating zone at 350 °C for 1 h. Figure 1 schematically illustrates the preparation process.

Fabrication of the MoS_2/p-Si photocathode

To achieve better contact, the backs of the MoS_2/p-Si samples were scratched using a blade, and an InGa alloy (Sigma-Aldrich, 99% purity) was subsequently coated on the scratched samples. Next, a copper wire was connected to the back of the MoS_2/p-Si samples using silver paste and dried on a hot plate at 50 °C for 1 h. Finally, epoxy resin was used to passivate the sample for subsequent PEC measurements. Figure S5 schematically shows the fabrication process.

Characterization

X-ray photoelectron spectroscopy (XPS) was performed using a K-alpha plus (ThermoFisher Scientific, USA) instrument under a vacuum of 1×10^{-5} mbar using Mg Kα radiation (1250 eV) and a constant pass energy of 50 eV. The crystal structures of the thin film samples were determined by X-ray diffraction (XRD) analysis (New D8-Advance, Bruker-AXS, Germany) with a Cu Kα target at 0.1542 nm. Raman spectra (LabRAM HR, Horiba Jobin Yvon, Japan) were obtained at an excitation wavelength of 515 nm. The field-emission scanning electron microscopy (FE-SEM, Zeiss 300 VP) images were obtained at an acceleration voltage of 50 kV. Transmission electron microscopy (TEM) was performed using a JEOL-2100F (Japan) instrument. Atomic force microscopy (AFM, XE-100/PSIA) was used to evaluate the roughness and thickness of the prepared thin films. The transmittance spectra of the thin films were examined by a UV-vis spectrophotometer (V-670).

Photoelectrochemical measurements

Electrochemical measurements were performed in 0.5 M H_2SO_4 using a three-electrode quartz electrochemical cell connected to a potentiostat (Ivium 5612, Netherlands). An Oriel 150 W solar simulator was used and calibrated to an output of 100 mW/cm^2 under AM 1.5 G 100 mW/cm^2 illumination. A scan rate of 10 mV/s was used for the 15 linear sweeps. EIS was conducted by applying a constant potential of −0.65 V relative to the open circuit potential with a sweeping frequency ranging from 250 kHz to 0.1 Hz with a 10 mV AC dither.

Acknowledgements

This research was supported by the Bio & Medical Technology Development Program (2018M3A9H1023141), the Creative Materials Discovery Program through the NRF funded by the Ministry of Science and ICT (2017M3D1A1039379), and the Basic Research Laboratory of the NRF funded by the Korean government (2018R1A4A1022647).

Author details

[1]School of Chemical Engineering and Materials Science, Integrative Research Center for Two-Dimensional Functional Materials, Institute of Interdisciplinary Convergence Research, Chung-Ang University, 84 Heukseok-ro, Dongjak-gu, Seoul 06974, Republic of Korea. [2]Institute of Research and Development, Duy Tan University, Da Nang 550000, Vietnam. [3]Department of Materials Science and Engineering, Research Institute of Advanced Materials, Seoul National University, Seoul, Republic of Korea. [4]Department of Materials Science and Engineering, Korea University, 145, Anam-ro Seongbuk-gu, Seoul 02841, Republic of Korea

Author contributions

A.H. and Q.V.L. contributed equally to this work. A.H. and Q.V.L. performed the synthesis of the materials and most of the characterization. A.H. and M.T. performed the device characterization. M.J.C. and T.H.L. analyzed the characterization of the materials. H.W.J. and S.Y.K. supervised the experiments and contributed to the manuscript preparation. H.W.J. and S.Y.K. initiated and directed the research. S.Y.K. conceived the idea and designed the experiments. All authors were involved in writing the manuscript.

Conflict of interest

The authors declare that they have no conflict of interest.

Supplementary information is available for this paper at https://doi.org/10.1038/s41427-019-0145-7.

Received: 7 March 2019 Revised: 21 May 2019 Accepted: 24 May 2019.
Published online: 6 September 2019

References

1. Hasani, A., Tekalgne, M., Van Le, Q., Jang, H. W. & Kim, S. Y. Two-dimensional materials as catalysts for solar fuels: hydrogen evolution reaction and CO_2 reduction. *J. Mater. Chem. A* **7**, 430–454 (2019).
2. Hasani, A. et al. Ammonia-sensing using a composite of graphene oxide and conducting polymer. *Phys. Status Solidi Rapid Res. Lett.* **12**, 1800037 (2018).
3. Li, X. & Zhu, H. Two-dimensional MoS_2: Properties, preparation, and applications. *J. Mater.* **1**, 33–44 (2015).
4. Hasani, A. et al. Poly (3, 4 ethylenedioxythiophene): poly (styrenesulfonate)/Iron (III) porphyrin supported on S and N Co-doped graphene quantum dots as a hole transport layer in polymer solar cells. *Sci. Adv. Mater.* **9**, 1616–1625 (2017).
5. Shim, Y.-S. et al. Synthesis of numerous edge sites in MoS_2 via SiO_2 nanorods platform for highly sensitive gas sensor. *ACS Appl. Mater. Interfaces* **10**, 31594–31602 (2018).
6. Choi, M. et al. Flexible active-matrix organic light-emitting diode display enabled by MoS_2 thin-film transistor. *Sci. Adv.* **4**, 8721 (2018).
7. Choi, G. J. et al. Polarized light-emitting diodes based on patterned MoS_2 nanosheet hole transport layer. *Adv. Mater.* **29**, 1702598 (2017).
8. Park, M. et al. MoS_2-nanosheet/graphene-oxide composite hole injection layer in organic light-emitting diodes. *Electron Mater. Lett.* **13**, 344–350 (2017).
9. Hasani, A. et al. The role of metal dopants in WS_2 nanoflowers in enhancing the hydrogen evolution reaction. *Appl. Catal., A.* **567**, 73–79 (2018).
10. Le, Q. V., Nguyen, T. P. & Kim, S. Y. UV/ozone-treated WS2 hole-extraction layer in organic photovoltaic cells. *Phys. Status Solidi Rapid Res. Lett.* **8**, 390–394 (2014).
11. Deng, S. et al. Phase modulation of (1T-2H)-$MoSe_2$/TiC-C shell/core arrays via nitrogen doping for highly efficient hydrogen evolution reaction. *Adv. Mater.* **30**, 1802223 (2018).
12. Shang, J., Cong, C., Wu, L., Huang, W. & Yu, T. Light sources and photodetectors enabled by 2D semiconductors. *Small Methods*, **2**, 1800019 (2018).
13. Zhou, C. et al. Self-driven metal–semiconductor–metal WSe_2 photodetector with asymmetric contact geometries. *Adv. Funct. Mater.* **28**, 1802954 (2018).
14. Li, X., Wu, S. & Zhu, Z. Band gap control and transformation of monolayer-MoS_2-based hetero-bilayers. *J. Mater. Chem. C.* **3**, 9403–9411 (2015).
15. Zhang, W. et al. High-gain phototransistors based on a CVD MoS_2 monolayer. *Adv. Mater.* **25**, 3456–3461 (2013).
16. Devers, E., Afanasiev, P., Jouguet, B. & Vrinat, M. Hydrothermal syntheses and catalytic properties of dispersed molybdenum sulfides. *Catal. Lett.* **82**, 13–17 (2002).
17. Fleischauer, P. D. & Bauer, R. Chemical and structural effects on the lubrication properties of sputtered MoS2 films. *Tribology Trans.* **31**, 239–250 (1988).
18. Li, M.-Y. et al. Epitaxial growth of a monolayer WSe_2-MoS_2 lateral pn junction with an atomically sharp interface. *Science* **349**, 524–528 (2015).
19. Walton, R. I., Dent, A. J. & Hibble, S. J. In situ investigation of the thermal decomposition of ammonium tetrathiomolybdate using combined time-resolved X-ray absorption spectroscopy and X-ray diffraction. *Chem. Mater.* **10**, 3737–3745 (1998).
20. Williams, J., DiCarlo, L. & Marcus, C. Quantum Hall effect in a gate-controlled pn junction of graphene. *Science* **317**, 638–641 (2007).
21. Deng, Y. et al. Black phosphorus–monolayer MoS_2 van der Waals heterojunction p–n diode. *ACS Nano* **8**, 8292–8299 (2014).
22. Liu, X. et al. High response, self-powered photodetector based on the monolayer MoS2/P–Si heterojunction with asymmetric electrodes. *Langmuir* **34**, 14151–14157 (2018).
23. Henning, A. et al. Charge separation at mixed-dimensional single and multilayer MoS_2/silicon nanowire heterojunctions. *ACS Appl. Mater. Interfaces* **10**, 16760–16767 (2018).
24. Yan, X. et al. High performance amplifier element realization via MoS_2/GaTe heterostructures. *Adv. Sci.* **5**, 1700830 (2018).
25. Hao, L. et al. Electrical and photovoltaic characteristics of MoS_2/Si pn junctions. *J. Appl. Phys.* **117**, 114502 (2015).
26. Wang, L. et al. MoS_2/Si heterojunction with vertically standing layered structure for ultrafast, high-detectivity, self-driven visible-near infrared photodetectors. *Adv. Funct. Mater.* **25**, 2910–2919 (2015).
27. Kwon, K. C. et al. Wafer-scale transferable molybdenum disulfide thin-film catalysts for photoelectrochemical hydrogen production. *Energy Environ. Sci.* **9**, 2240–2248 (2016).
28. Salvatore, G. A. et al. Fabrication and transfer of flexible few-layers MoS_2 thin film transistors to any arbitrary substrate. *ACS Nano* **7**, 8809–8815 (2013).
29. Yang, H. et al. Highly scalable synthesis of MoS_2 thin films with precise thickness control via polymer-assisted deposition. *Chem. Mater.* **29**, 5772–5776 (2017).
30. Van Ngoc, H., Qian, Y., Han, S. K. & Kang, D. J. PMMA-etching-free transfer of wafer-scale chemical vapor deposition two-dimensional atomic crystal by a water soluble polyvinyl alcohol polymer method. *Sci. Rep.* **6**, 33096 (2016).
31. Ma, D. et al. Etching-free transfer of wafer-scale MoS_2 films. *arXiv Prepr. arXiv* **1501**, 00786 (2015).
32. Ding, Q. et al. Efficient photoelectrochemical hydrogen generation using heterostructures of Si and chemically exfoliated metallic MoS_2. *J. Am. Chem. Soc.* **136**, 8504–8507 (2014).
33. Tsai, M.-L. et al. Monolayer MoS_2 heterojunction solar cells. *ACS Nano* **8**, 8317–8322 (2014).
34. Liu, K.-K. et al. Growth of large-area and highly crystalline MoS_2 thin layers on insulating substrates. *Nano Lett.* **12**, 1538–1544 (2012).
35. Xi, Y. et al. Fabrication of MoS_2 thin film transistors via selective-area solution deposition methods. *J. Mater. Chem. C.* **3**, 3842–3847 (2015).
36. Dumcenco, D. et al. Large-area epitaxial monolayer MoS_2. *ACS Nano* **9**, 4611–4620 (2015).
37. Smithe, K. K., Suryavanshi, S. V., Muñoz Rojo, M., Tedjarati, A. D. & Pop, E. Low variability in synthetic monolayer MoS_2 devices. *ACS Nano* **11**, 8456–8463 (2017).
38. Zhang, X. et al. Phonon and Raman scattering of two-dimensional transition metal dichalcogenides from monolayer, multilayer to bulk material. *Chem. Soc. Rev.* **44**, 2757–2785 (2015).
39. Jia, X. et al. Sulfur–silicon bond activation catalysed by Cl/Br ions: waste-free synthesis of unsymmetrical thioethers by replacing fluoride catalysis and fluorinated substrates in SN Ar reactions. *Green. Chem.* **16**, 3444–3449 (2014).
40. Kargar, A. et al. NiO_x-Fe_2O_3-coated p-Si photocathodes for enhanced solar water splitting in neutral pH water. *Nanoscale* **7**, 4900–4905 (2015).
41. Benson, J., Li, M., Wang, S., Wang, P. & Papakonstantinou, P. Electrocatalytic hydrogen evolution reaction on edges of a few layer molybdenum disulfide nanodots. *ACS Appl. Mater. Interfaces* **7**, 14113–14122 (2015).